Spatially resolved acoustic spectroscopy additive manufacturing – towards online inspection

Don Milesh Pieris[1,2], Rikesh Patel[1,2], Paul Dryburgh[1,2], Matthias Hirsch[1,2], Wenqi Li[1], Steve D. Sharples[1], Richard J. Smith[1], Adam T. Clare[2], Matt Clark[1]

[1]Optics and Photonics, Faculty of Engineering, University of Nottingham, Nottingham, UK
[2]Advanced Component Engineering Laboratory (ACEL), Faculty of Engineering, University of Nottingham, Nottingham, UK

Abstract

High-integrity engineering applications such as aerospace will not permit the incorporation of components containing any structural defects. The current generation of additive manufacturing platforms yield components with relatively high levels of defects. The in-line inspection of the components built using additive can provide closed-loop feedback and vary build parameters during fabrication to minimise such defects. This article reviews the capability of spatially resolved acoustic spectroscopy to be used as an in-line inspection tool for detecting the changes in parts induced due to variations in build parameters. The first considers the build laser power and the second varies the laser scan strategy used to build the component. Using the detected probe light intensity map and the measured surface acoustic velocity, the detection of surface defects, subsurface defects and component microstructure can be measured.

1. Introduction

As Additive Manufacturing (AM) processes develop and start to be used in more high-value industries such as biomedical, automotive and aerospace sectors, the need to inspect and understand the material properties of the manufactured components will continue to grow [1], [2]. Selective Laser Melting (SLM) is an AM process capable of manufacturing metallic components with high precision and fine microstructure [3].

The relationship between the microstructure and mechanical properties of superalloys capable of performing at high temperatures is well understood [4]. The microstructure of AM components, however, vary significantly to those manufactured using more traditional methods such as casting. This is due to the drastic thermal gradients that occur during the build process of each layer. This variable microstructure combined with the propensity of current-class build systems to manufacture parts with high levels of structural defects, leads to parts with unpredictable and often inferior mechanical performance. For this reason, new research is required towards detecting and controlling the microstructure of AM components [3].

The layer by layer nature of the AM process provides a unique opportunity for an intermediate layer inspection to take place, to generate quasi-volumetric datasets. The primary requirement for such an inspection would be that it is both non-contact and

non-destructive. A range of ultrasonic, optical and thermal Non-Destructive Testing (NDT) techniques have been considered for such an intermediate layer inspection in the past [5]–[7]. It was demonstrated that they were capable of detecting simple structural defects such as cracks and pores but failed to classify them and provide any information on the component microstructure. From this, there is a distinct need for an NDT technique capable of probing the material properties of the component and providing the AM machine user with some understanding of the microstructure of the fabricated component.

Spatially Resolved Acoustic Spectroscopy (SRAS) is a laser ultrasonic technique which uses Surface Acoustic Waves (SAWs) to probe the elastic properties of the sample to generate a mechanical response, additionally generating a separate optical image. Previously, SRAS has been used to measure the grain orientation of large-grained materials such as nickel, titanium and silicon [8]–[10]. As an NDT technique SRAS is uniquely placed to address many of the challenges instigated by SLM. It has capability to inform upon microstructural texture of the part [11], the ability to differentiate between surface and sub-surface defects [12], and potentially measure on rough surfaces [13]. The technique and instrumentation is described in greater depth in previous work [14]. This article focuses on how SRAS can be used to detect a wide range of defects found within SLM components such as cracks and pores and how it can provide an insight into component microstructure.

2. Instrumentation

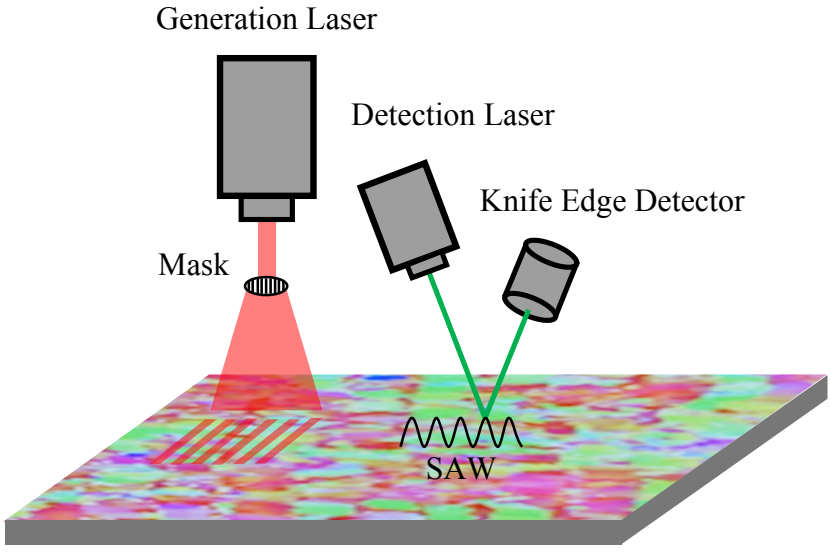

Figure 1. Schematic outlining the 1064 nm generation laser, mask used to define the wavelength, 532 nm detection laser and KED. The acoustic wavelength of the current SRAS system is set to 24 µm. The acoustic generation patch was 200 µm in diameter and optical detection spot was 8 µm in diameter.

The primary elements required to build a SRAS system are: a pulsed generation laser (typically a Q-Switched YAG at 1064 nm, repetition rate 2 kHz, pulse energy 10 µJ); a mask used to define the acoustic wavelength; a detection laser (continuous wave at532 nm, typically 60 mow at the sample); and a Knife Edge Detector (KED). The generation

laser in conjunction with mask rapidly heats the sample within its thermoelastic regime. This generates (SAWs) of which the wavelength, λ, is defined by the spacing between the lines on the mask. The frequency of the SAW, *f*, travelling across the sample is measured by monitoring the perturbation of the detection laser via the KED. Having set the acoustic wavelength and measured the corresponding frequency, the SAW velocity, *v*, is then calculated by Equation 1. A more in-depth description of how the system operates can be found in previously published literature [14]–[16].

$$v = f\lambda \quad \text{.....(1)}$$

3. Methodology

The following section investigated the capability of the SRAS instrument to detect changes to a component within an SLM build context. This was carried out using two experiments designed to vary the SLM build parameters.

The first experiment varied the laser power incident on the sample during manufacture. The SRAS system was then used to identify the effect of this change. These samples were also used to investigate the capability of the system to detect surface defect density.

The second experiment aimed to keep all build parameters constant and vary the build laser scan strategy. The SRAS instrument was then used to identify these changes on the surface of the sample. Furthermore, the data was used to measure and characterise the defects found on the surface of the samples.

4. SAW Velocity and Defect Density Variation Study

4.1. Sample Preparation

Smith et al. manufactured eleven samples with the aim of detecting changes to the build laser power used [12]. The samples were manufactured using a Renishaw AM250 SLM machine which had a laser spot size of 70 μm and used a Ti-6Al-4V powder feedstock. All the samples were 10 x 10 x 10 mm cubes manufactured with a layer thickness of 30 μm, hatch spacing of 75 μm and a scan speed of 600 mm/s. The build laser power was varied across the samples from 70 W to 200 W. The samples were then polished to a mirror finish and inspected using SRAS.

4.2. Results

This section presents the results obtained from the specimens outlined above using the SRAS instrument. The detection of changes to build parameters was discussed and correlated to changes in either the SRAS optical return or velocity measurement. Following that, defects within the component were detected.

Due to the method in which SRAS data was gathered, a typical SRAS scan provides two distinct datasets. The optical return outlined in Figure 2 (left) and the velocity map shown in Figure 2 (right).

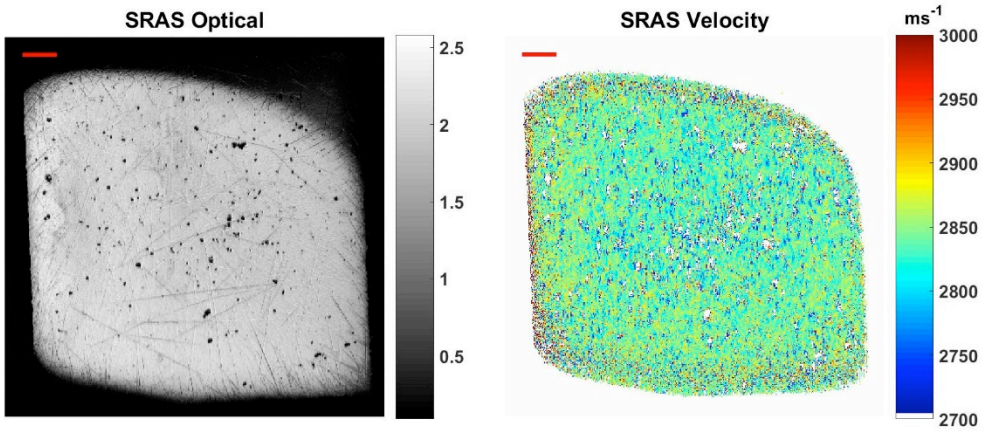

Figure 2. Example SRAS dataset from sample number 8 (140W), (Left) Optical return, showing many surface breaking defects. The optical dataset is a voltage measurement, based on the light level returned to the KED. (Right) Velocity return of SRAS, defects can also be discerned from the dataset, but critically the microstructural texture development can be observed (1 mm scale bar).

4.2.1. Variations in Surface Defect Density and SAW Velocity

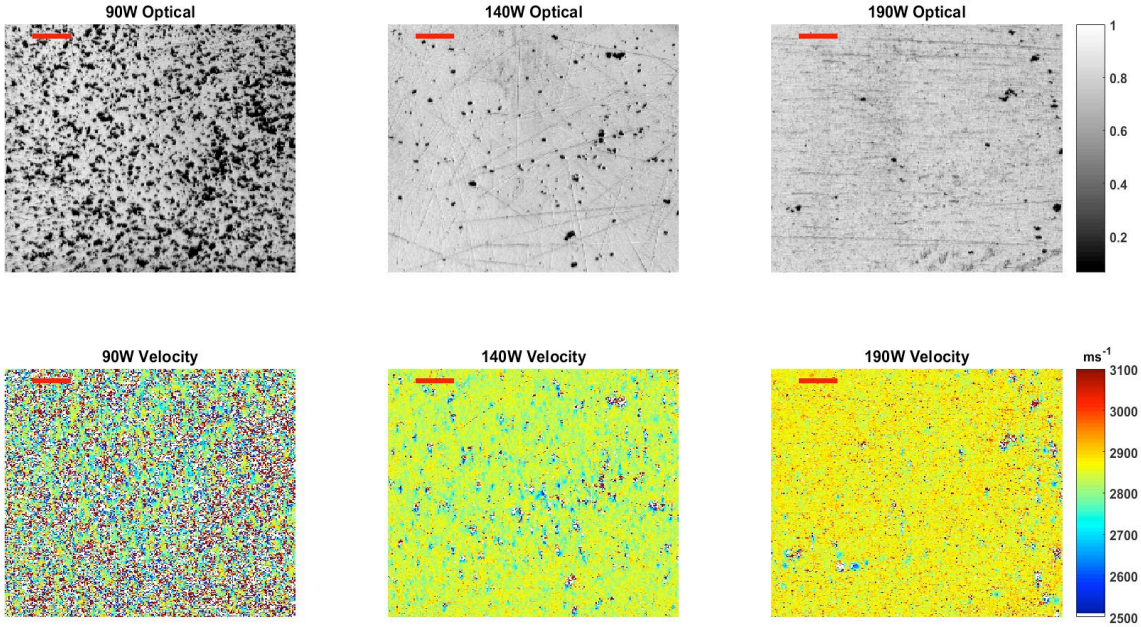

Figure 3. (Top) Optical return providing an indication of surface defects but no information regarding material properties. (Bottom) Velocity return showing changes across the range of samples (0.5mm scale bar).

The top row of Figure 3 illustrated how the SRAS optical return provided indications of surface defects such as scratches, cracks and pores. The velocity maps in bottom row of Figure 3 illustrated the richer data stream of acoustic data, which gave some indication of change across the samples manufactured with varying build powers.

The mean velocity was calculated for each sample inspected using SRAS and the trend outlined in Figure 4 was observed. It was clear that as the incident laser power increased across each build, the mean velocity also increased. This increase, however, was not linear and stabilised at the higher energy inputs. It is worth noting, although not fully investigated it is hypnotised this could either be due to a reduction in porosity, or to the development of a preferential grain orientation.

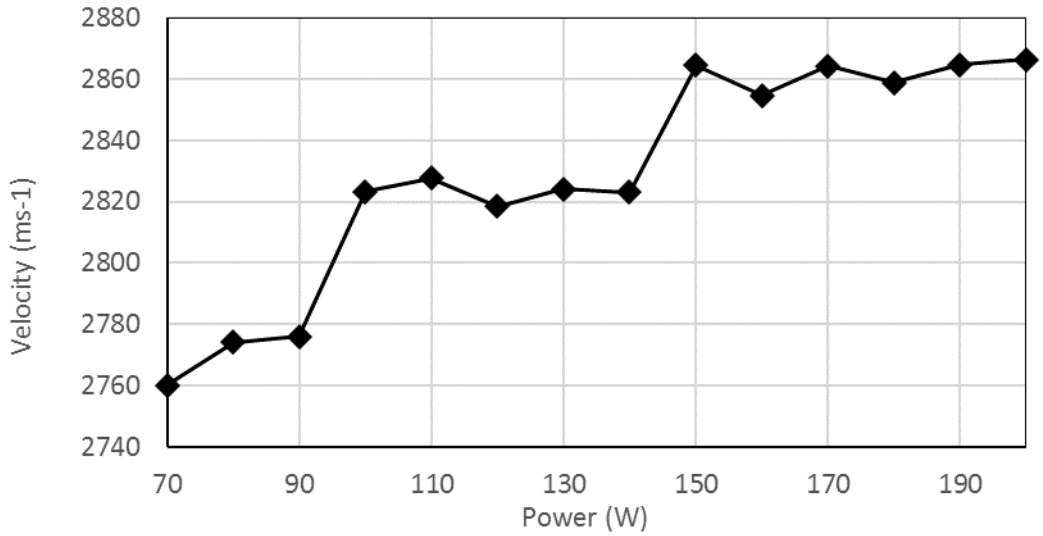

Figure 4. Relationship between input laser power and mean SAW velocity.

4.2.2. Surface and Subsurface Pore Detection

Figure 5 (a) illustrated the optical SRAS image of the 190W sample. A small section of this sample was inspected closer in (b). The optical defects observed here were confirmed using the SEM image in (c). The velocity map of the sample was shown in
Figure 5 (d) and a closer view in (e). Several acoustic dropouts were observed in the upper half of Figure 5 (e) which were not observed in the optical images (a)-(c). The XCT image in
Figure 5 (f) was of the region just below that of figure (b) and (e). The darker area in the XCT image correlated well with the top half of the velocity image but did not correspond with the SRAS optical and SEM images, confirming the acoustic drop was due to a subsurface feature.

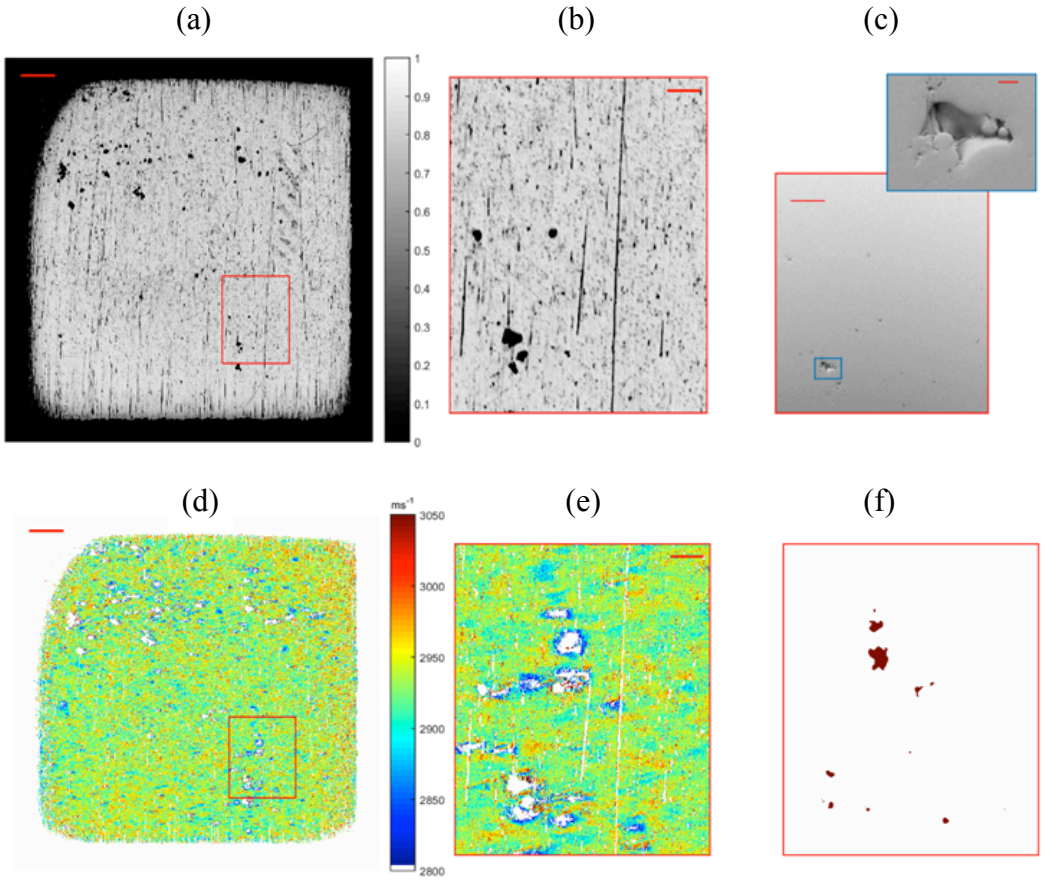

Figure 5. 190 W sample; (a) Optical return (1 mm scale bar), (b) close-up view of surface defect (250 µm scale bar), (c) SEM image of surface defect (250 µm scale bar) and inset zoom of defect (25 µm scale bar), (d) velocity map (1 mm scale bar), (e) close-up view of surface and potential subsurface defects (250 µm scale bar), (f) XCT image of confirmed subsurface defects at approximately 60 µm.

4.3. **Discussion**

Varying the laser power directly varied the energy incident on the sample fabricated. Based on the SRAS results presented in section 4.2.1 it was clear that the variation of laser power - and thereby energy input - caused changes within the component, in this case in the SAW velocity measured. The laser power also in this case caused changes to the surface defect density, clearly observed in the SRAS optical return.

The combination of the SRAS optical and velocity results in section 4.2.2 provided an indication that some subsurface defects can be observed. The top middle velocity map in Figure 6 illustrated the typical SAW velocity data within a range of 3050 ms^{-1} and 2800 ms^{-1}. The Lamb wave dispersion curve (top left) for a 24 µm wavelength in titanium illustrates this velocity range using a green box. When the SRAS data was processed using a wider velocity range (centre bottom figure) it was clear that lower velocities which corresponded to the a_0 mode (top right figure) were present. With respect to the cross section in the bottom right figure, it is possible that the SAW wave

transformed in to a Lamb wave in the thin region above the pore. This in conjunction with the XCT data presented in
Figure 5 (f) confirmed that these were indeed subsurface pores.

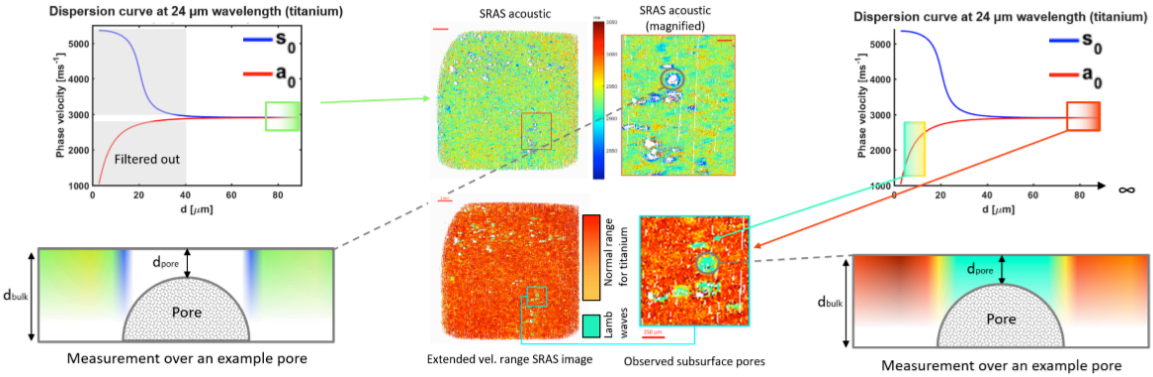

Figure 6 Difference between the normal velocity range detected using SRAS for surface waves and the extended velocity range used for the detection of Lamb waves.

5. Microstructure Variation Study

5.1. Sample Preparation

Hirsch et al. manufactured a second set of samples but this time with the aim of detecting changes to the hatch pattern used by the build laser [11]. In this case, a Realizer SLM50 was used with the nickel super alloy CM247-LC feedstock. The laser power was set to 100 W at a speed of 400 mm/s with a hatch spacing of 50 µm and a laser spot size of 50 µm. Each build layer consisted of four equally sized square islands. The angle of the scan lines within these islands were varied across the four samples manufactured. The hatch angles used were 00º, 15º, 30º, and 45º. The following figure outlines a schematic drawing of the 00º and 30º samples.

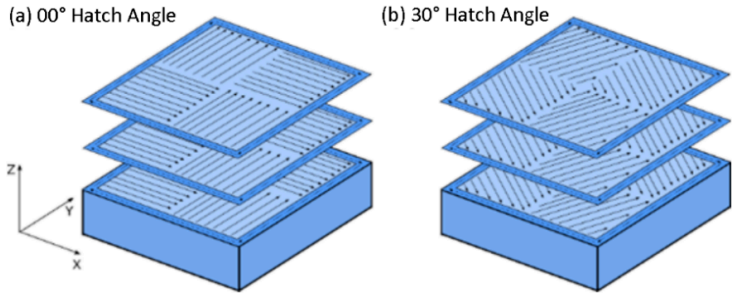

Figure 7 Schematic drawing (a) of 00º and (b) 30º hatch angle samples with equally sized square islands, illustrating how the scan lines are consistently aligned to the set angle across each layer.

5.2. Results

This section presents the effect changes to the hatch pattern had on the SRAS results obtained. This data was processed further to classify the defects found on the surface of the sample. Finally changes to the component microstructure was discussed with relation to the SRAS velocity plots and island boundaries defined during the build of the samples.

5.2.1. **Defect Size and Density Variation**

The following figure indicated how the SRAS optical return (Figure 8 top row) could be used to clearly identify surface defects such as cracks and pores. The bottom row velocity maps illustrate the wide range of velocity variations observed using SRAS. It was clear that the changes to the hatch angle used during manufacture could be detected using SRAS optical as variation in the crack/pore density and velocity maps as changes to SAW velocity.

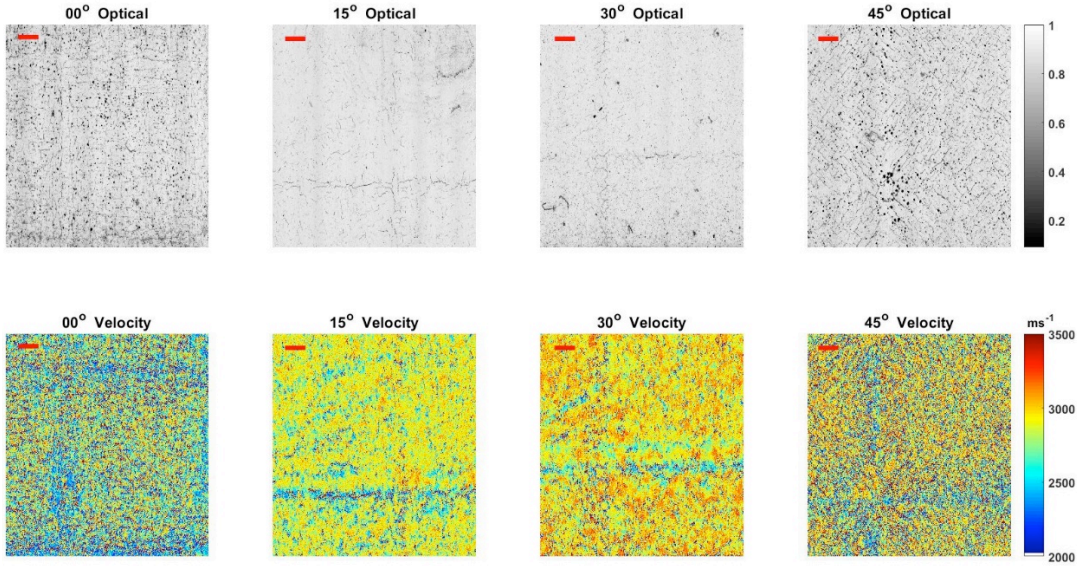

Figure 8 (Top row) Optical images of SRAS scans of varying hatch angle samples showing some variations in porosity. (Bottom row) Velocity maps of varying hatch angle samples showing clear indications of island boundaries as regions low velocity (scale bar 0.5 mm).

This data was used in conjunction with the information presented in Table 1 to classify the defects observed.

Table 1: Primary defects in selective laser melting, adapted from Everton et al. [18].

Metal Powder Bed Defect	Description	Typical sizes	Reference
Spherical pores	Entrapped gas pores within the bulk of the material. Material dependent.	5-20 µm	[19], [20]
Acicular pores	Pores in between layers of the AM process.	50-500 µm	[19], [20]
Unfused powder	The melt pool varies in size and unfused powder is present.	Satellite powder clumps: 100-150 µm.	[21]
Cracking	Cracks can be within the component or a disconnection of the part from the baseplate is seen.	Parts on bed: residual stress in the range of materials yield strength.	[22], [23]

Using a combination of the SRAS velocity and optical data, a binary dataset of the defects observed on the 0º hatch angle sample was obtained. Following some image processing on this data set, parameters such as the pore location, area, diameter, width and perimeter were extracted.

The calculated defect aspect ratio was used to distinguish between cracks and pores, where cracks would have a higher aspect ratio. The circularity was used to classify pores, where a gas pore would have relatively high circularity. Similarly, the defect count (Figure 9 right) could be used as an acceptance criterion, where components with a given number of defects above a certain threshold would not be accepted.

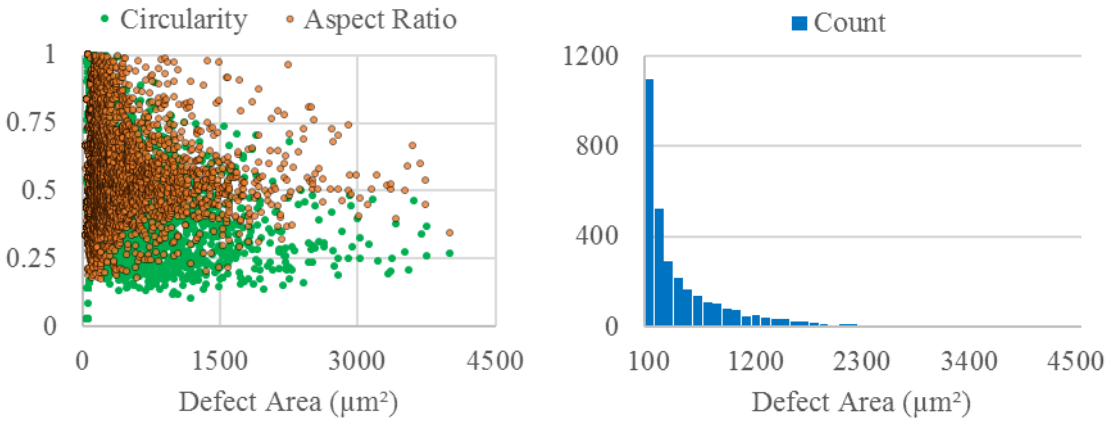

Figure 9 (Left) Defect data used to calculate the normalised circularity and aspect ratio. (Right) The number of defects found as ranked by their area.

Once several categories of defects were observed - based on the information presented in Table 1 - the cause of defects can be identified, and action can be taken to prevent them in subsequent layers. Armed with information such as the location, size and shape of the defect, a repair strategy could be implemented [17].

As a comparison to the SRAS optical data, optical microscopy images were obtained of the surface defects found on the surface of the samples in section **Error! Reference source not found.**. From Figure 10 the SRAS optical dataset regularly suggests higher

defect rates than suggested by traditional optical microscopy. This was primarily due to the sensitivity of the laser-based measurement, this made the SRAS optical dataset more sensitive to subtle features but also made it more sensitive to normal variations in background reflectivity. Distinguishing between this will be an important step in the industrialisation of SRAS.

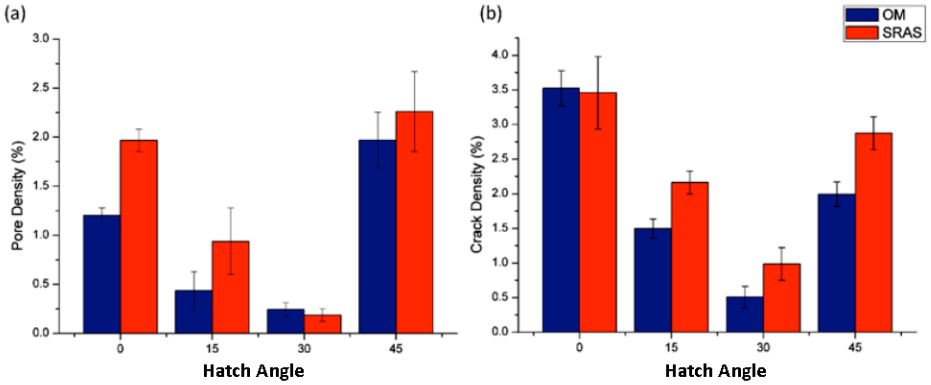

Figure 10 Comparison of surface cracks and pore density using SRAS and optical microscopy.

The results presented above showed that the SRAS instrument was not only capable of detecting typical mechanical defects such as cracks and pores, but it was also sensitive to the small changes in the component microstructure. This was seen from the square island boundaries observed in the velocity plots of Figure 8 as lower velocity regions.

5.2.2. Microstructure Variation

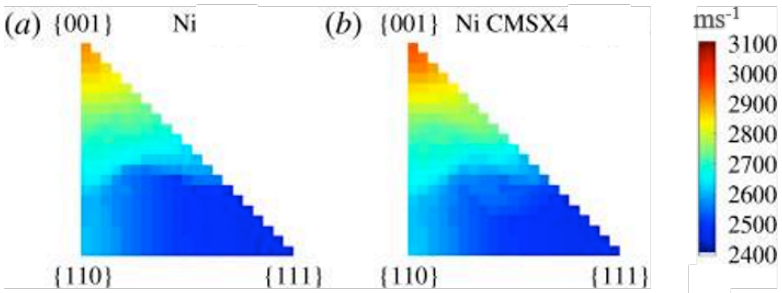

Figure 11 Average velocity maps of all plane families of nickel and a nickel super alloys, which were calculated based on the elastic constants determined by (a) Salama et al. [24]**, (b) Zhang et al.** [25]**.**

Carter et al. utilised electron backscatter diffraction to assess the predominate crystalline orientations in similarly processed CM247LC [26]. The central regions of the hatching islands were seen to have elongated grains with a strong {0 0 1} orientation. The island boundaries had a finer grain and more chaotic texture with {1 0 1} and {1 1 1} orientations dominating. Li et al. have previously reported on the relationship between material elastic properties, crystalline orientation and SAW velocity [16]. Using a similar approach, the average SAW velocity was calculated form the alloys elastic constants, as shown in Figure 11. Comparing this to the velocity plots given in Figure 8, suggested good agreement with the findings of Carter et al.

On top of the small changes detected across the island boundaries, one highly significant anomaly was detected. A small uncharacteristic line of low velocity was

observed inside the north east island of the 30º sample, this was mirrored in the optical images (Figure 12). Upon closer inspection of the build taking place frame by frame it was observed how the scan laser overshot its assigned island on a layer. This was confirmed to be what was observed in the SRAS velocity and optical data of the 30º sample (Figure 12 (d)).

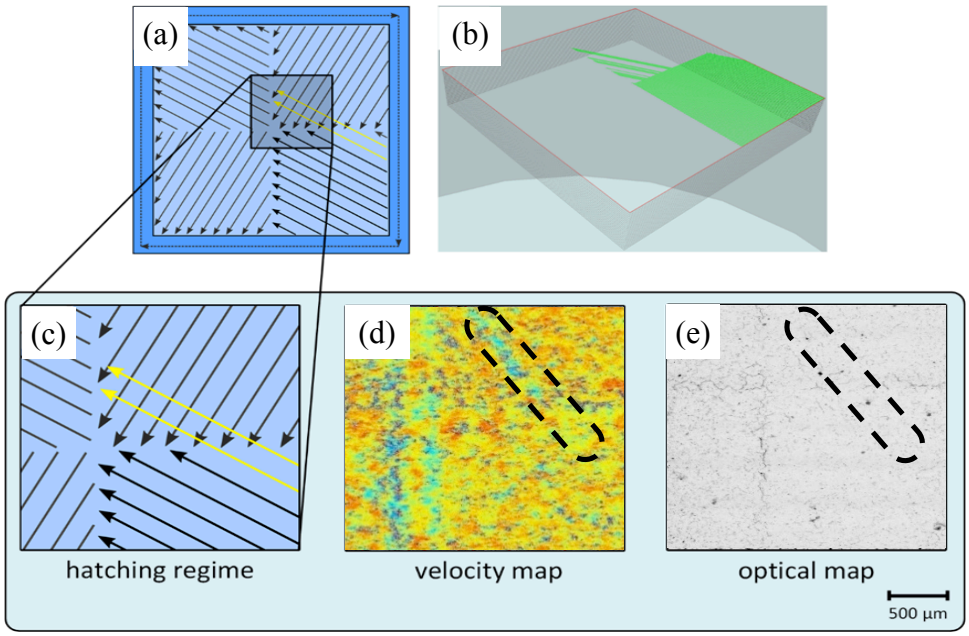

Figure 12 (a) Plan view of overall scan strategy for 30º sample, (b) 3D schematic of the scan error, (c) zoomed in image of plan view of the error in scan strategy, (d) error in laser scan strategy detected using SRAS velocity and (e) SRAS Optical.

The authors acknowledge the 'elephant in the room' is the applicably of the technique to optically rough surfaces. Continuing development of the Speckle Knife Edge Detector (SKED) [27], promises to herald a practical solution and early results will be presented in forthcoming work. This along with opto-mechanical integration provides the greatest challenges to the realisation of an in-line SRAS instrument for SLM inspection.

6. Conclusions

Based on the results discussed above it was clear that the SRAS instrument was capable of detecting changes to laser power and hatching strategy. On top of this it was also shown that the SRAS instrument can be used to count, size and classify defects commonly found in SLM manufactured parts. This combination means that this instrument could be used as part of a feedback loop capable of varying build parameters on the fly to minimise defects and optimise parameters such as laser power and scan strategy for a given component geometry. Hirsch et al. conducted a preliminary study into the feasibility of localised reworking of recognised defects, based on SRAS generated data [17].

Furthermore, it was also observed that the instrument was capable of detecting some changes to the component microstructure. If implemented as part of an inline inspection tool with some further development and an increase in the spatial resolution of the acoustic dataset could potentially be used to tailor the microstructure of the component being fabricated.

7. References

[1] L. C. Zhang, D. Klemm, J. Eckert, Y. L. Hao, and T. B. Sercombe, "Manufacture by selective laser melting and mechanical behavior of a biomedical Ti-24Nb-4Zr-8Sn alloy," *Scr. Mater.*, vol. 65, no. 1, pp. 21–24, 2011.

[2] K. N. Amato *et al.*, "Microstructures and mechanical behavior of Inconel 718 fabricated by selective laser melting," *Acta Mater.*, vol. 60, no. 5, pp. 2229–2239, 2012.

[3] L. Thijs, K. Kempen, J. P. Kruth, and J. Van Humbeeck, "Fine-structured aluminium products with controllable texture by selective laser melting of pre-alloyed AlSi10Mg powder," *Acta Mater.*, vol. 61, no. 5, pp. 1809–1819, 2013.

[4] I. A. Essienubong, O. Ikechukwu, P. O. Ebunilo, and E. Ikpe, "Material Selection for High Pressure (HP) Turbine Blade of Conventional Turbojet Engines," *Am. J. Mech. Ind. Eng. Ikpe Aniekan Essienubong Am. J. Mech. Ind. Eng.*, 2016.

[5] H. Rieder, M. Spies, J. Bamberg, and B. Henkel, "On- and Offline Ultrasonic Inspection of Additively Manufactured Components," pp. 1–8, 2016.

[6] M. Islam, T. Purtonen, H. Piili, A. Salminen, and O. Nyrhilä, "Temperature profile and imaging analysis of laser additive manufacturing of stainless steel," *Phys. Procedia*, vol. 41, pp. 835–842, 2013.

[7] H. Krauss, T. Zeugner, and M. F. Zaeh, "Layerwise monitoring of the Selective Laser Melting process by thermography," *Phys. Procedia*, vol. 56, no. C, pp. 64–71, 2014.

[8] R. Smith, S. Sharples, W. Li, M. Clark, and M. Somekh, "Orientation imaging using spatially resolved acoustic spectroscopy," *J. Phys. Conf. Ser.*, vol. 353, p. 012003, 2012.

[9] P. C. Series, "Orientation Characterisation of Aerospace Materials by Spatially Resolved Acoustic Spectroscopy," no. October 2016, pp. 1–6, 2014.

[10] R. Patel, W. Li, R. J. Smith, S. D. Sharples, and M. Clark, "Orientation imaging of macro-sized polysilicon grains on wafers using spatially resolved acoustic spectroscopy," *Scr. Mater.*, vol. 140, pp. 67–70, 2017.

[11] M. Hirsch *et al.*, "Meso-scale defect evaluation of selective laser melting using spatially resolved acoustic spectroscopy," *Proc. R. Soc. A Math. Phys. Eng. Sci.*, vol. 473, no. 2205, p. 20170194, 2017.

[12] R. J. Smith, M. Hirsch, R. Patel, W. Li, A. T. Clare, and S. D. Sharples, "Spatially resolved acoustic spectroscopy for selective laser melting," *J. Mater. Process. Technol.*, vol. 236, pp. 93–102, 2016.

[13] S. O. Achamfuo-Yeboah, R. A. Light, and S. D. Sharpies, "Optical detection of ultrasound from optically rough surfaces using a custom CMOS sensor," *J. Phys. Conf. Ser.*, vol. 581, p. 012009, 2015.

[14] R. J. Smith, W. Li, J. Coulson, M. Clark, M. G. Somekh, and S. D. Sharples, "Spatially resolved acoustic spectroscopy for rapid imaging of material microstructure and grain orientation," *Meas. Sci. Technol.*, vol. 25, no. 5, p. 055902, 2014.

[15] S. D. Sharples, M. Clark, and M. G. Somekh, "Spatially resolved acoustic spectroscopy for fast noncontact imaging of material microstructure.," *Opt. Express*, vol. 14, no. 22, pp. 10435–10440, 2006.

[16] W. Li, S. D. Sharples, R. J. Smith, M. Clark, and M. G. Somekh, "Determination

of crystallographic orientation of large grain metals with surface acoustic waves," vol. 132, no. 2, 2016.
[17] M. Hirsch *et al.*, "Targeted rework strategies for powder bed additive manufacture," *Addit. Manuf.*, vol. 19, no. November, pp. 127–133, 2018.
[18] S. K. Everton, M. Hirsch, P. Stravroulakis, R. K. Leach, and A. T. Clare, "Review of in-situ process monitoring and in-situ metrology for metal additive manufacturing," *Mater. Des.*, vol. 95, pp. 431–445, 2016.
[19] S. Tammas-Williams, H. Zhao, F. Léonard, F. Derguti, I. Todd, and P. B. Prangnell, "XCT analysis of the influence of melt strategies on defect population in Ti-6Al-4V components manufactured by Selective Electron Beam Melting," *Mater. Charact.*, 2015.
[20] L. Thijs, F. Verhaeghe, T. Craeghs, J. Van Humbeeck, and J. P. Kruth, "A study of the microstructural evolution during selective laser melting of Ti-6Al-4V," *Acta Mater.*, vol. 58, no. 9, pp. 3303–3312, 2010.
[21] H. . Niu and I. T. . Chang, "Instability of scan tracks of selective laser sintering of high speed steel powder," *Scr. Mater.*, vol. 41, no. 11, pp. 1229–1234, 1999.
[22] P. Mercelis and J.-P. J. Kruth, "Residual stresses in selective laser sintering and selective laser melting," *Rapid Prototyp. J.*, vol. 12, no. 5, pp. 254–265, 2006.
[23] M. F. Zaeh and G. Branner, "Investigations on residual stresses and deformations in selective laser melting," *Prod. Eng.*, vol. 4, no. 1, pp. 35–45, 2010.
[24] A. Salama, K Alers, G, "Third-order elastic modulus of pure nickel and some dilute copper-nickel alloys," in *IEEE Transactions on sonics and ultrasonics*, 1969, p. 28.
[25] X. Zhang, P. R. Stoddart, J. D. Comins, and A. G. Every, "High-temperature elastic properties of a nickel-based superalloy studied by surface Brillouin scattering," *J. Phys. Condens. Matter*, vol. 13, no. 10, pp. 2281–2294, 2001.
[26] L. N. Carter, C. Martin, P. J. Withers, and M. M. Attallah, "The influence of the laser scan strategy on grain structure and cracking behaviour in SLM powder-bed fabricated nickel superalloy," *J. Alloys Compd.*, vol. 615, pp. 338–347, 2014.
[27] S. D. Sharples, R. A. Light, S. O. Achamfuo-Yeboah, M. Clark, and M. G. Somekh, "The SKED: speckle knife edge detector," *J. Phys. Conf. Ser.*, vol. 520, no. 1, p. 012004, 2014.